

TIME-FREQUENCY ANALYSIS OF BROADBAND SOUND PULSE PROPAGATION IN 3-D OCEANIC WAVEGUIDES

Frederic Sturm, Julien Bonnel

▶ **To cite this version:**

Frederic Sturm, Julien Bonnel. TIME-FREQUENCY ANALYSIS OF BROADBAND SOUND PULSE PROPAGATION IN 3-D OCEANIC WAVEGUIDES. ECUA 2012, Jul 2012, Edinburgh, United Kingdom. hal-00738752

HAL Id: hal-00738752

https://ensta-bretagne.hal.science/hal-00738752

Submitted on 5 Oct 2012

HAL is a multi-disciplinary open access archive for the deposit and dissemination of scientific research documents, whether they are published or not. The documents may come from teaching and research institutions in France or abroad, or from public or private research centers.

L'archive ouverte pluridisciplinaire **HAL**, est destinée au dépôt et à la diffusion de documents scientifiques de niveau recherche, publiés ou non, émanant des établissements d'enseignement et de recherche français ou étrangers, des laboratoires publics ou privés.

TIME-FREQUENCY ANALYSIS OF BROADBAND SOUND PULSE PROPAGATION IN 3-D OCEANIC WAVEGUIDES

Frédéric Sturm Laboratoire de Mécanique des Fluides et d'Acoustique, UMR CNRS 5509, Ecole Centrale de Lyon, 36 avenue Guy de Collongue, 69134 Ecully Cedex, France. Email: frederic.sturm@ec-lyon.fr

Julien Bonnel LabSTICC / TOMS, UMR CNRS 6285, ENSTA Bretagne (UEB), 2 rue François Verny, 29806 Brest Cedex 9, France. Email: julien.bonnel@ensta-bretagne.fr

1 INTRODUCTION

When considering low-frequency sources, the oceanic environment can act as a very dispersive waveguide, especially in shallow-water long-range sound wave propagation. One efficient tool for studying dispersion effects is based on time-frequency (TF) analysis of the received signals using a single receiver [1,2] . However, theses studies only considered two-dimensional (2-D) waveguides. In the present paper, TF analysis is used to study the propagation of low-frequency broadband pulses in three-dimensional (3-D) shallow-water waveguides. In particular, the paper focuses on the 3-D ASA wedge benchmark for which the received signals present characteristic modal structures including multiple mode arrivals. Indeed, it is well known that, due to the presence of a tilted bottom, a single propagating mode can have two distinct arrivals on a single receiver located in the across-slope direction. One objective of the present study is to show that TF analysis can be a suitable tool to better understand and easily illustrate this phenomenon.

The paper is organized as follows. The 3-D ASA wedge benchmark is first recalled in Sec. 2. The simulated time signals are computed using a fully 3-D parabolic equation based code. The TF analysis is detailed in Sec. 3. The 2-D signals are first analyzed. Then comes the TF analysis for the 3-D signals. In particular, the spectrograms reveal that the second arrival of a given mode looks like the first one but is reversed in time. This observation is explained using mode-ray analogies. The paper ends with some concluding remarks.

2 TIME SERIES FOR THE WEDGE-SHAPED WAVEGUIDE

We consider the 3-D ASA wedge benchmark (three-dimensional extension of the original 2-D ASA wedge benchmark [3]). An isotropic point source is placed at a depth of 40 m in an oceanic environment which consists of a lossless homogeneous water layer (sound speed: 1500 m/s, density: 1 g/cm^3) overlying a lossy half-space sediment bottom (sound speed: 1700 m/s, density: 1.5 g/cm^3, and aborption: 0.5 dB/λ). No shear energy is assumed in the sediment. Using cylindrical coordinates, with z the depth (increasing downwards) below the ocean surface, θ the azimuthal (bearing) angle, and r the horizontal range from the source, the wedge-like tilted water/sediment interface is described by the surface $\{z = h(r, \theta)\}$ where

$$h(r, \theta) = 200 \left(1 - \frac{r \cos \theta}{4000} \right).$$

The water/sediment interface makes an angle of 2.86° with respect to the ocean surface at both $\theta = 0^\circ$ (upslope direction) and and $\theta = 180^\circ$ (downslope direction) and is invariant along the $\theta = 90^\circ$ and $\theta = 270^\circ$ azimuthal directions. Note that the water depth at the source location is 200 m.

Time series at several ranges in the across-slope direction (receiver depth: 40 m) corresponding to fully-3-D computations are plotted in Fig. 1. In the same figure are plotted the 2-D solutions corresponding to the equivalent 2-D environment for comparison. The source signal is a Hanning-weighted

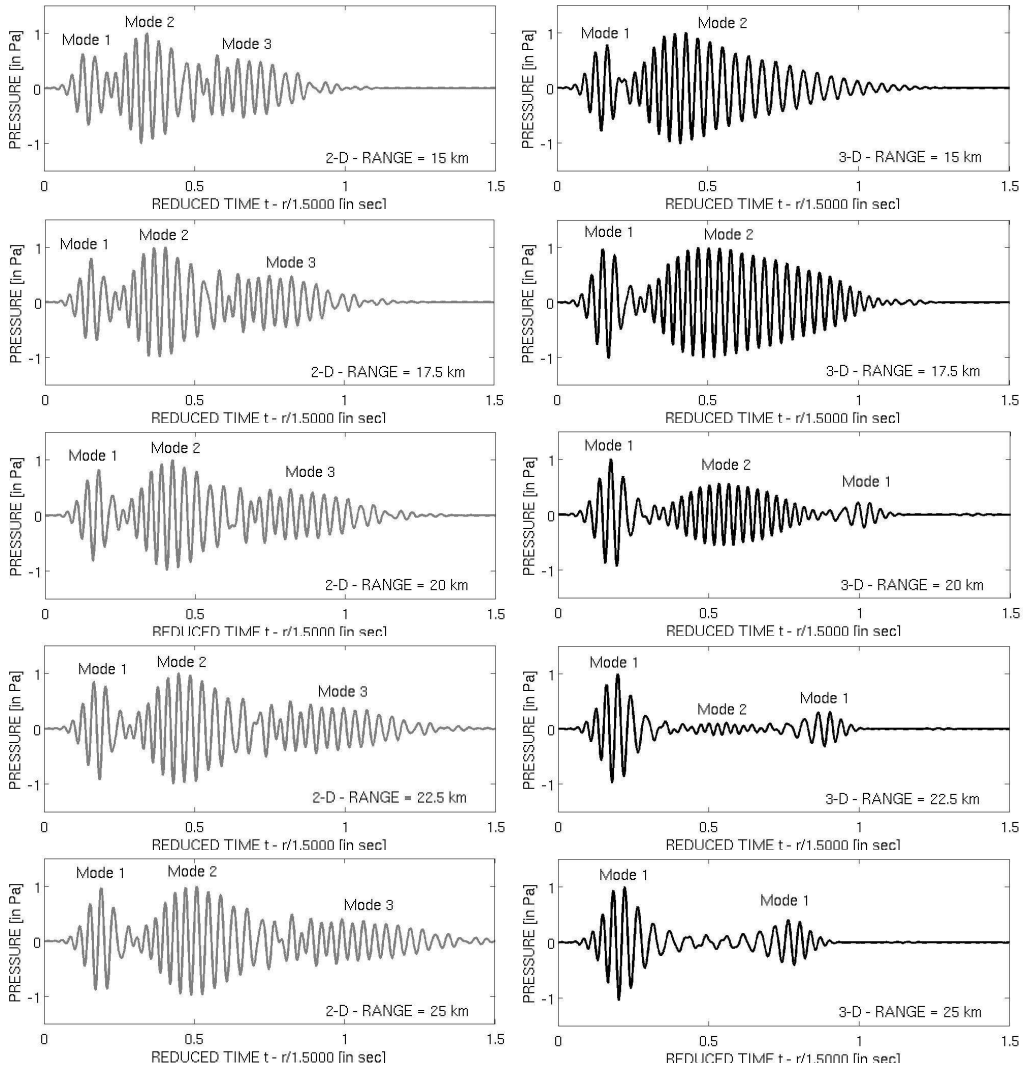


Figure 1: Time series (receiver depth: 40 m) at several ranges in the across-slope direction corresponding to 2-D (left panel) and fully-3-D computations (right panel) using the 3-D PE code 3DWAPE. The simulated signals were scaled appropriately to compensate for cylindrical spreading.

four-period sine pulse wave given by $\mathcal{S}(t) = \frac{1}{2}(1 - \cos(2\pi f_c t/4)) \sin(2\pi f_c t)$ if $0 \leq t \leq 4/f_c$ and zero elsewhere (the initial pulse length is 0.16 s), with center frequency $f_c = 25$ Hz. Source pulse and source spectrum are displayed in Fig. 2. The numerical results were obtained using the 3-D parabolic equation based model 3DWAPE [4] coupled with a Fourier synthesis technique to handle the time dependence of the source signal. The computation domain in the across-slope direction is range-independent and is thus seen by the 2-D model like a classical Pekeris waveguide. The 200 m deep waveguide leads to the existence of three propagating modes at 25 Hz. Therefore, considering the broadband source pulse with a central frequency of 25 Hz, the 2-D propagating signal splits up in three distinct wave packets, the dispersion of each individual modal wave packet increasing as the receiver moves out in range. According to the group velocity curves displayed in Fig. 3, we observe that, for each propagating mode, the first arrivals consist of high-frequency contributions, whereas the late arrivals have a more low-frequency content (above the Airy phase) (*e.g.*, for mode 1, the group velocity is 1493 m/s at 30 Hz and 1487 m/s at 20 Hz).

The time series corresponding to the 3-D solutions show a different modal structure, giving evidence of well-known 3-D effects for each propagating mode, *e.g.* multiple arrivals of each mode, being

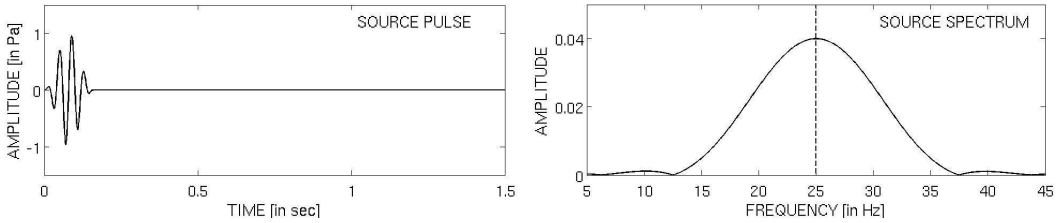


Figure 2: Source pulse (left) and its spectrum (right)

distinguishable at some ranges, then merging together and progressively disapearing as we move out across-slope (mode shadow zone). The reader is referred to Ref. [5] for a more detailed description of the 3-D effects experienced by the propagating modes. A closer examination of the 3-D signals reveals that the frequency content of a given wave packet varies in range (see for instance mode-2 wave packet at ranges of 15 km and 17.5 km). This effect, which appears first for higher modes, is known as the range dependence of the cut-on frequency (or, equivalently, the frequency dependence of mode cut-off range) of a propagating mode. Of particular interest, we can observe, looking at the first 3-D modal arrival associated to mode 1, that high frequencies arrive before low frequencies (similar to the 2-D situation) whereas it is the contrary for the second 3-D arrival of mode 1 (low frequencies arrive before high frequencies). As clearly shown in the next section, the time-frequency analysis allows a better visualization and understanding of this effect.

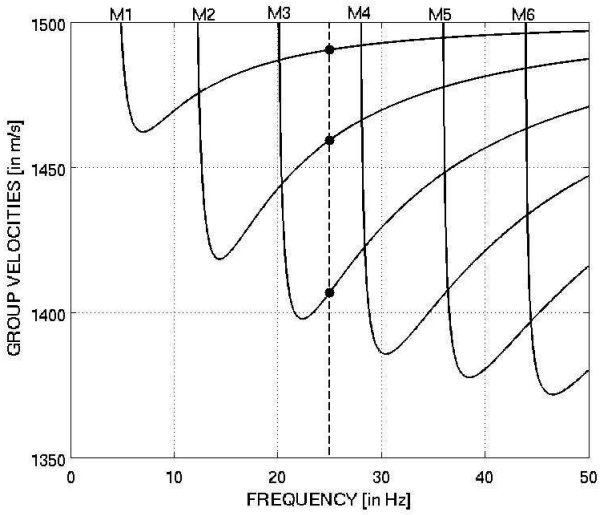


Figure 3: Group velocities for the Pekeris waveguide (across-slope direction; 2-D case).

3 TIME-FREQUENCY ANALYSIS

Let $s(t)$ denote the time signal received on a single receiver after propagating in the wedge-shaped oceanic waveguide described above, computed using either 2-D calculation or fully-3-D calculation. Following Ref. [6], the time signal $s(t)$ can be brought into the TF domain using short time Fourier transform (STFT)

$$\mathrm{STFT}\{s\}(t,f) = \int_{-\infty}^{\infty} s(\tau) h^*(\tau - t) \mathrm{e}^{-\mathrm{i}2\pi f t} \mathrm{d}\tau,$$

where $h(t)$ is the window function centered around zero.

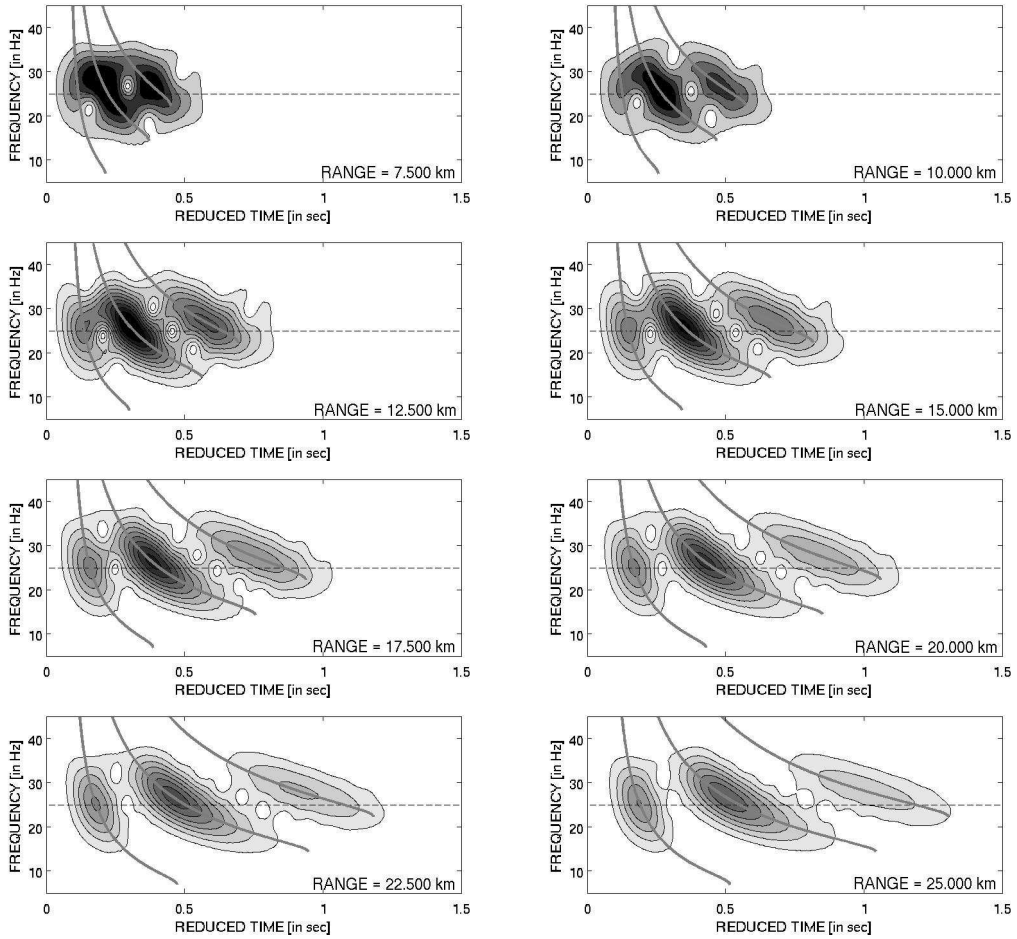


Figure 4: Spectrograms of the received signals at several across-slope distances (from 7.5 to 25 km) coresponding to 2-D PE computations. Source and receiver depths are both 40 m. Theoretical time-frequency dispersion curves are plotted (thick gray curves) for comparison.

Figure 4 shows the spectrograms of the received signals at a 40 m depth (corresponding to 2-D computations) after propagation across slope for several ranges. The gray curves superimposed on the spectrograms in each panel correspond to the theoretical dispersion curves of the three propagating modes, given by

$$t_m(f) = r/c_{\mathrm{g},m}(f), \quad 1 \leq m \leq 3,$$

where r denotes the source-receiver range and $c_{\mathrm{g},m}(f)$ denotes the group velocity of mode m at frequency f. Hence, $t_m(f)$ corresponds to the arrival time of mode m at frequency f. Note that, for each mode, the part of the theoretical dispersion curve corresponding to frequencies below the Airy phase is not displayed. The STFTs of Fig. 4 follow the form of the dispersion curves, spread according to the window function used. We observe that at large ranges, modes are well separated in the TF domain. For relatively smaller source-receiver ranges, the modes tend to overlap (generating interferences) and become thus more hardly distinguishable. For a given mode m, the spectrograms confirm that the early arrivals of mode m consist of high-frequency contributions, whereas the late arrivals have a low-frequency content.

The spectrograms corresponding to fully-3-D computations are shown in Fig. 5 for the same source-receiver ranges considered in Fig. 4. They correspond to a receiver at a constant 40 m depth in the across-slope direction. Several observations can be made. As in Fig. 4, the spectrograms allow to separate the modal arrivals. Unlike in 2-D, one mode can now have two distinct arrivals. The second modal arrival can be well separated in time from the first modal arrival (see for instance ranges 20

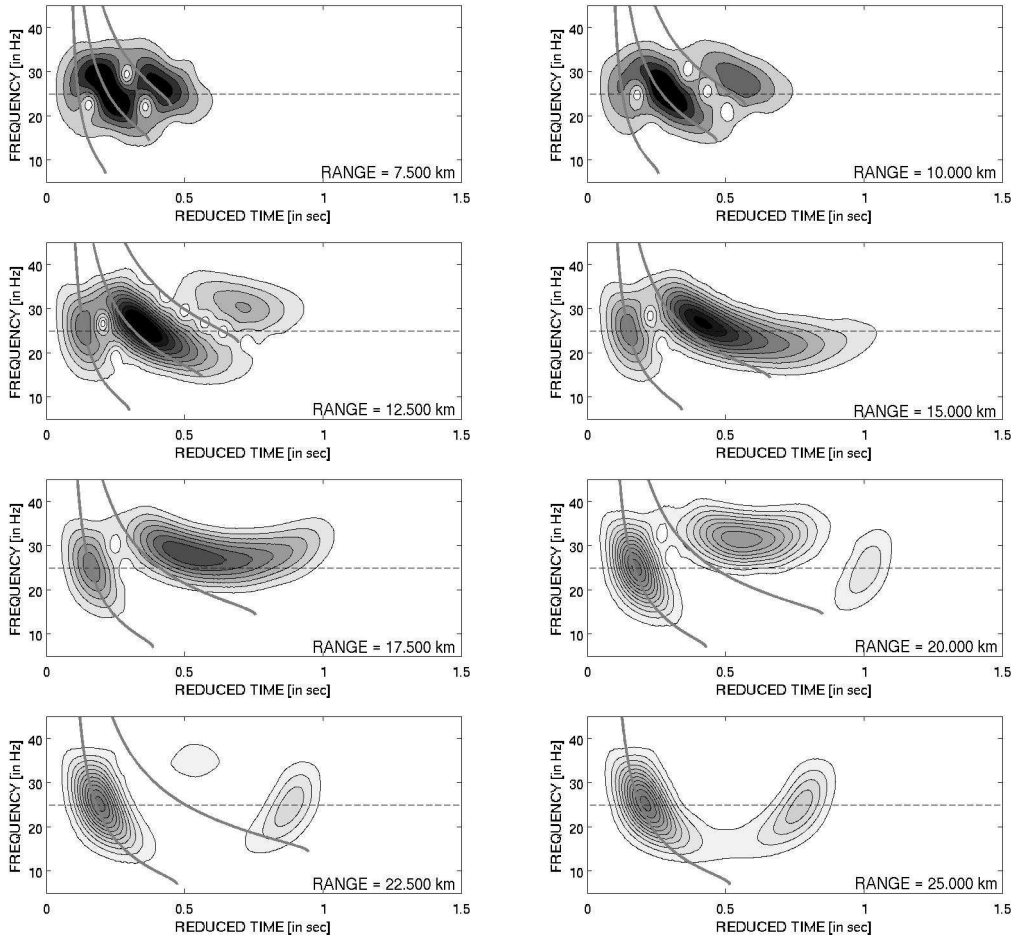


Figure 5: Spectrograms of the received signals at several across-slope distances (from 7.5 to 25 km) coresponding to fully-3-D PE computations. Source and receiver depths are both 40 m. Theoretical time-frequency dispersion curves are plotted (thick gray curves) for comparison.

to 25 km for mode 1) but can also be merged with the first modal arrival (see ranges 15 to 20 km for mode 2). For each mode and for each source-receiver range, the shape in the TF domain of the first modal arrival follows the shape of the corresponding 2-D predictions shown in Fig. 4, with higher frequencies arriving first. The second modal arrival, when present, looks like the first one but is reversed in time, low frequencies arriving now first. We note that at short distances (*e.g.*, at $r = 7.5$ km), each mode corresponds to an almost direct propagation between the source and the receiver (nearly no 3-D effects). As a consequence, its shape in the TF domain deviates only slightly from the 2-D theoretical dispersion curves (plotted in gray for comparison). However, as we move out in range, we observe a now more pronounced deviation of the first arrival of the mode in the TF domain from the 2-D dispersion curves. Note also that for a given mode, the low frequencies disappear before the high frequencies. This phenomenon is due to horizontal refraction effects, and is known as range dependence of the cut-on frequency (see discussion in Sec. 2).

All these effects can be explained easily using mode-ray analogies as follows. First of all, recall that at a fixed frequency, a given mode can be viewed as rays propagating along hyperbolic paths in the horizontal plane, being horizontally refracted towards regions of deeper water. A modal ray, travelling first upslope (*i.e.*, launched obliquely towards the wedge apex), turns back downslope, thus intersecting the across-slope direction at some range, leading to a shadow zone region across-slope at a sufficiently large distance (the so-called mode cut-off range). The cut-off range of a given mode is shifted out in range with increasing frequency (see for instance in Refs. [7–11]). Considering a

	Receiver range: 20 km			Receiver range: 25 km		
Frequency [in Hz]	ϕ_0 [in deg]	L_{ϕ_0} [in m]	t_{ϕ_0} [in s]	ϕ_0 [in deg]	L_{ϕ_0} [in m]	t_{ϕ_0} [in s]
15	6.4	20 046.41	13.56	–	–	–
	19.7	20 643.63	14.06	–	–	–
20	3.6	20 013.86	13.47	5.2	25 038.02	16.87
	21.5	20 883.22	14.18	15.2	25 470.65	17.26
25	2.4	20 005.84	13.43	3.2	25 011.44	16.79
	22.1	21 017.32	14.24	16.7	25 638.88	17.35
30	1.7	20 002.85	13.40	2.25	25 004.19	16.76
	22.3	21 098.21	14.27	17.2	25 733.36	17.38
35	1.3	20 001.53	13.39	1.7	25 001.19	16.73
	22.4	21 158.97	14.29	17.6	25 809.15	17.41

Table 1: Characteristics (for several frequencies within the frequency band of the source pulse) of the modal rays associated to mode 1 launched from the source and connected with a receiver in the across-slope direction. The angle ϕ_0 denotes the initial launch angle ($\phi_0 = 90^\circ$ points up-slope and $\phi_0 = 0^\circ$ points across-slope) of a modal eigenray, L_{ϕ_0} denotes the length of a modal eigenray path and t_{ϕ_0} denotes its travel time.

broadband source pulse, this means that the extinction of a given modal wave packet, instead of being abrupt, takes place in an extended region along the across-slope direction. This is what the spectrograms of Fig. 5 show for modes 2 and 3; a larger maximum computation range (≈ 45 km) would be required to see the same effect for mode 1 (see in Ref. [12]). Assuming that, at a given frequency f, the receiver range is less than the cut-off range of mode m, and depending on its position along the across-slope direction, a receiver may see either one single arrival of mode m, or two distinct arrivals of the same mode m. In the latter case, the first mode arrival corresponds to a ray launched at a low horizontal angle $\phi_{0,1}$ with respect to the across-slope direction, and the second to a ray launched at a higher horizontal angle $\phi_{0,2} > \phi_{0,1}$. Note that the first and second arrivals of the same mode are often referred to in the literature as 'direct arrival' and 'echo'. The paths of these 'first' and 'second' eigenrays depend on frequency and source-receiver ranges. For example, the characteristics of the modal rays associated to mode 1 launched from the source and connected with a receiver in the across-slope direction are given in Table 1 for several frequencies within the frequency band of the source pulse and for two source-receiver ranges. Corresponding eigenray paths (for selected frequencies 20 Hz and 30 Hz) are shown in Fig. 6. Note that there are no data at 15 Hz for a receiver range of 25 km (which is beyond the cut-off range of mode 1 at 15 H).

Let us analyze first the frequency content of the first arrival (*i.e.*, the 'direct arrival') of a mode. For a given mode m and a fixed source-receiver range, $\phi_{0,1}$ decreases as frequency increases. In other words, as can be seen in Fig. 6, the higher frequency paths deviate less and less from the straight line connecting the source and the receiver as frequency increases. Therefore, the leading edge of the first arrival of mode m consists of high-frequency contributions and the trailing edge consists of low-frequency contributions. This is similar to what was observed for the single arrival of each propagating mode for the 2-D Pekeris waveguide (see the 2-D spectrograms shown in Fig. 4). For instance, at a source-receiver range of 20 km, $\phi_{0,1} = 3.6^\circ$ (arrival time: 13.47 s) at 20 Hz and $\phi_{0,1} = 1.7^\circ$ (arrival time: 13.40 s) at 30 Hz for mode 1. The 30 Hz eigenray arrives thus 0.07 s before the 30 Hz eigenray at 20 km. It is worth noting that, for each frequency, the bending of the eigenray paths, which is relatively low at small source-receiver ranges, increases as the receiver moves out in range. This explains why the shape of the first arrival of each mode deviates in the TF domain from the corresponding theoretical 2-D dispersion curve.

Let us analyze now the frequency content of the second arrival (*i.e.*, the 'echo') of a mode. For a given mode m and a fixed source-receiver range, $\phi_{0,2}$ now increases as frequency increases (*e.g.,* see in Fig. 6 at both receiver ranges). The corresponding eigenray path penetrates farther into the shallower portion of the wedge-shaped waveguide as frequency increases. The low-frequency paths are thus longer than the high-frequency paths, and low frequencies arrive now before high frequencies. The

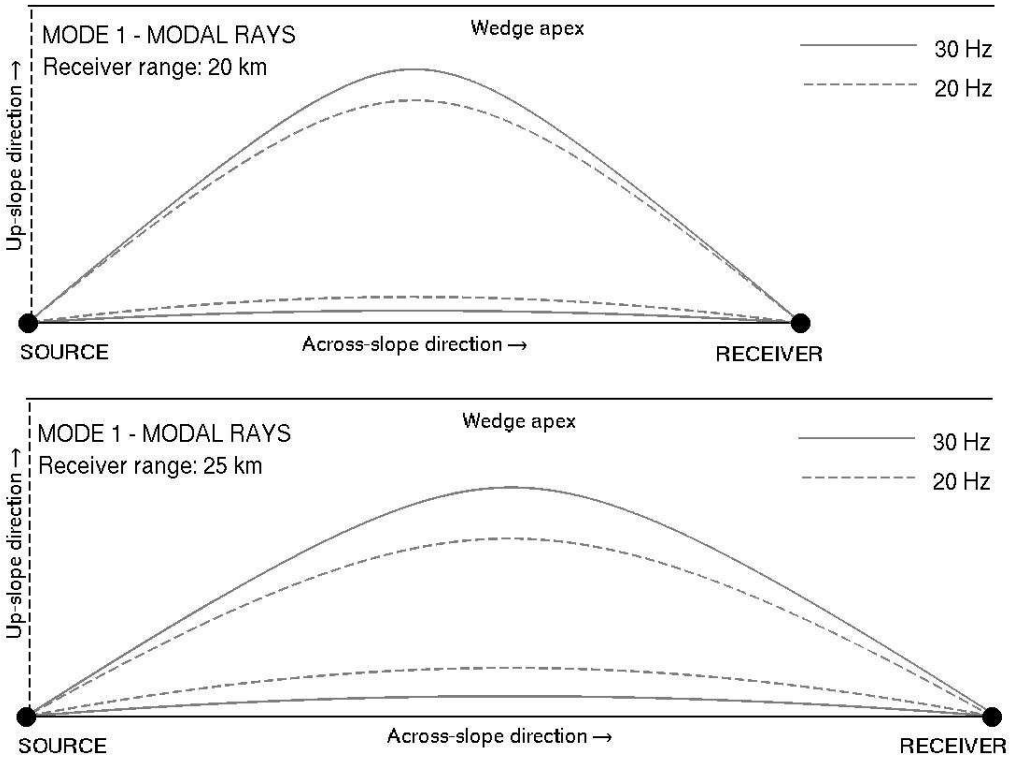


Figure 6: Modal eigenray paths corresponding to mode 1 for a receiver range of (a) 20 km and (b) 25 km. On each panel, two frequencies are considered: 20 Hz (dashed curves) and 30 Hz (continuous curves).

second arrival of a mode appears thus reversed in time in the TF domain. For instance, at a source-receiver range of 20 km, $\phi_{0,2} = 21.5°$ (arrival time: 14.18 s) at 20 Hz and $\phi_{0,2} = 22.3°$ (arrival time: 14.27 s) at 30 Hz for mode 1. Unlike the first arrival of mode 1, the 20 Hz eigenray for the second arrival of mode 1 arrives 0.09 s before the corresponding 30 Hz eigenray.

4 CONCLUDING REMARKS

It has been shown in this paper that the time-frequency analysis allows to fully characterize the dispersion of multiple mode arrivals in a specific synthetic 3-D oceanic waveguide, the 3-D wedge benchmark. In this case, time-frequency analysis is especially helpful when a single receiver is available. At a given range, it provides an accurate description of 3-D modal dispersion. As a perspective, we will explore sound propagation problems with other more complicated 3-D bottom profiles (*e.g.,* canyon, seamont, trench). Another perspective of such studies is to develop new signal processing methods allowing single-receiver geoacoustic inversion in 3-D oceanic environments.

REFERENCES

1. J. Bonnel, C. Gervaise, P. Roux, B. Nicolas, and J. I. Mars. Modal depth function estimation using time-frequency analysis. *J. Acoust. Soc. Am.*, 130(1): pp. 61–71, 2011.

2. J. Bonnel, C. Gervaise, P. Roux, B. Nicolas, and J. I. Mars. Single-receiver geoacoustic inversion using modal reversal. *J. Acoust. Soc. Am.*, 131(1): pp. 119–128, 2012.

3. F. B. Jensen and W. A. Kuperman. Sound propagation in a wedge-shaped ocean waveguide with a penetrable bottom. *J. Acoust. Soc. Am.*, 67: pp. 1564–1566, 1980.

4. F. Sturm. Numerical simulations with 3DWAPE considering shallow water range-dependent environments. *J. Acoust. Soc. Am.*, 105(5): pp. 2334–2335, 2001.

5. F. Sturm. Numerical study of broadband sound pulse propagation in three-dimensional ocean waveguides. *J. Acoust. Soc. Am.*, 117(3): pp. 1058–1079, 2005.

6. F. Hlawatsch and G. Boudreaux-Bartels. Linear and quadratic time-frequency signal representations. *IEEE Signal Processing Magazine*, 9(2): pp. 21–67, 1992.

7. E. K. Westwood. Broadband modeling of the three-dimensional penetrable wedge. *J. Acoust. Soc. Am.*, 92(4): pp. 2212–2222, 1992.

8. C. H. Harrison. Acoustic shadow zones in the horizontal plane. *J. Acoust. Soc. Am.*, 65: pp. 56–61, 1979.

9. M. J. Buckingham. Theory of three-dimensional acoustic propagation in a wedgelike ocean with a penetrable bottom. *J. Acoust. Soc. Am.*, 82(1): pp. 198–210, 1987.

10. S. A. L. Glegg and J. R. Yoon. Experimental measurements of three-dimensional propagation in a wedge-shaped ocean with pressure-release boundary conditions. *J. Acoust. Soc. Am.*, 87(1): pp. 101–105, 1990.

11. S. A. L. Glegg, G. B. Deane, and I. G. House. Comparison between theory and model scale measurements of three-dimensional sound propagation in a shear supporting penetrable wedge. *J. Acoust. Soc. Am.*, 94: pp. 2334–2342, 1993.

12. F. Sturm. Investigation of 3-d benchmark problems in underwater acoustics: a uniform approach. In *Proceedings of the 9th European Conference on Underwater Acoustics (Paris, France), edited by M. E. Zakharia, co-editors: D. Cassereau and F. Luppé*, vol. 2, pp. 759–764, 2008.